Supplementary Materials for

Wafer-scale high-κ HfO_2 dielectric films with sub-5-Å equivalent oxide thickness for 2D MoS_2 transistors

Songge Zhang[1,2,3†], Tao Zhang[1,4†], Hua Yu[1], Tong Li[1], Xiuzhen Li[5,6], Chenyang Cui[5,6], Yuchao Zhou[1], Hailing Guo[7], Shuopei Wang[1], Dongfeng Zheng[1], Liangfeng Huang[1], Liqi Bai[3], Su Liu[2], Cheng Shen[8], Wei Yang[5,6], Luojun Du[5,6], Dongxia Shi[5,6], Lede Xian[1,9,10*], Xiaoming Tao[2], Yang Chai[3], Na Li[1*] & Guangyu Zhang[1,5,6*]

[1]Songshan Lake Materials Laboratory, Dongguan, Guangdong 523808, China

[2]Research Institute for Intelligent Wearable Systems, School of Fashion and Textiles, The Hong Kong Polytechnic University, Hong Kong 999077, China

[3]Department of Applied Physics, The Hong Kong Polytechnic University, Hong Kong 999077, China

[4]Department of Materials Science and Engineering, City University of Hong Kong, Hong Kong, 999077, China

[5]Beijing National Laboratory for Condensed Matter Physics and Institute of Physics, Chinese Academy of Sciences, Beijing 100190, China

[6]School of Physical Sciences, University of Chinese Academy of Sciences, Beijing 100190, China

[7]Department of Engineering, University of Cambridge, Cambridge CB2 1PZ, United Kingdom

[8]School of Physics, University of Electronic Science and Technology of China, Chengdu 610054, China

[9]Tsientang Institute for Advanced Study, Zhejiang 310024, China

[10]Max Planck Institute for the Structure and Dynamics of Matter, Luruper Chaussee 149, 22761 Hamburg, Germany

†These authors contribute equally.

*Corresponding authors. Email: xianlede@sslab.org.cn; lina@sslab.org.cn; gyzhang@iphy.ac.cn

Supplementary Note 1:

The mobility bandgaps were measured with the help of inverse participation ratio (IPR) of densities of states, which can reflect the localization degree of densities of states (DOS).

$$IPR(\mathrm{eV}) = \frac{\sum_{N} DOS_i(eV)^2}{(\sum_{N} DOS_i(eV))^2}$$

Where $DOS_i(eV)$ represents the DOS of each atom. In amorphous structures, due to the disorder, the band edges often show localized electronic states[1-3]. Compared with crystalline structure, the bandgap (E_g) becomes mobility bandgap (ME_g), and the valence band maximum and conduction band minimum are switched as valence band mobility edge (VBME) and conduction band mobility edge (CBME). Thus, here we use IPR to analyze the band edge of amorphous structure. In our research, we set the mid energetic positions of IPR in valence band and conduction band as the valence band edge and conduction band edge, respectively. The mobility band edges and mobility bandgap are summarized in Supplementary Tables 1-6.

Supplementary Note 2:

Besides the amorphous HfO_2 systems, we also examined the variation of bandgaps in crystalline HfO_2 systems, as shown in Supplementary Figs. 24-27. In Supplementary Fig. 28, the results indicate that the bandgaps of crystalline HfO_2 gradually decrease with the increasing defect concentration for both DFT functionals. The primary difference between two functionals lies in the fact that the PBE functional tends to underestimate the bandgaps, a behaviour that has also been reported in previous studies[4,5]. To further elucidate the influence of functionals choice, we compared the band structures of perfect crystalline HfO_2 calculated using HSE06[6] and PBE functional, as shown in Supplementary Fig. 29, the comparison reveals that the HSE functional preserves the overall band-structure features obtained with PBE, but results in a larger separation between the valence and conduction bands. Therefore, considering the significantly higher computational cost of HSE06 functional, we calculate the amorphous HfO_2 systems with the PBE functional.

For calculations performed using the Vienna *ab initio* Simulation Package (VASP)[7], The Kohn-Sham wavefunctions and the charge density are expanded in a plane-wave basis set with an energy cutoff of 500 eV. The convergence criterion is 5×10^{-5} eV and 0.05 eV/Å for energy and force, respectively. The Brillouin zone is sampled with the k-mesh with spacing of 0.12 $Å^{-1}$.

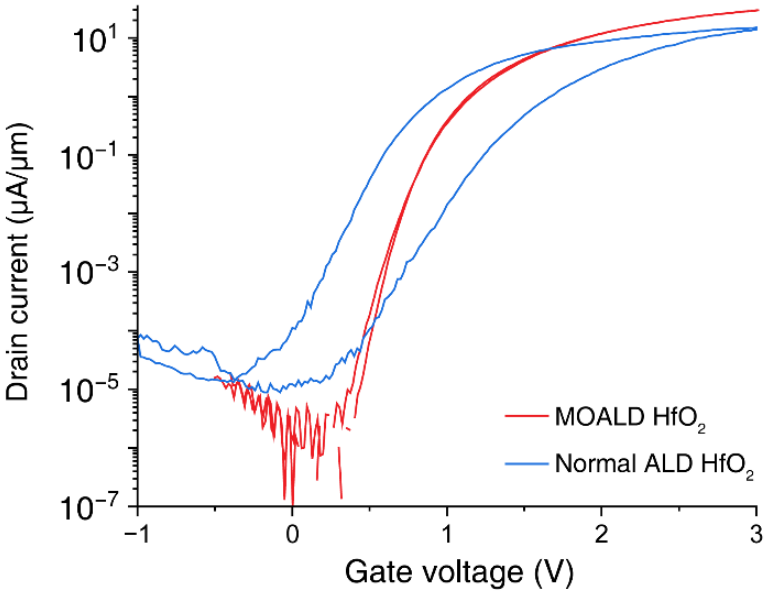

Supplementary Fig. 1 | Transfer curves of monolayer MoS_2 FETs with MOALD and normal HfO_2 as dielectrics, respectively. The thicknesses for two HfO_2 films are all 5 nm.

The hysteresis at 10 nA/μm is ~5 mV for FET with MOALD HfO_2 while 550 mV for FET with normal HfO_2. The on/off ratio with MOALD HfO_2 is an order of magnitude higher than that with normal HfO_2. This demonstrates the higher quality of high-κ dielectrics improve the performance of FETs.

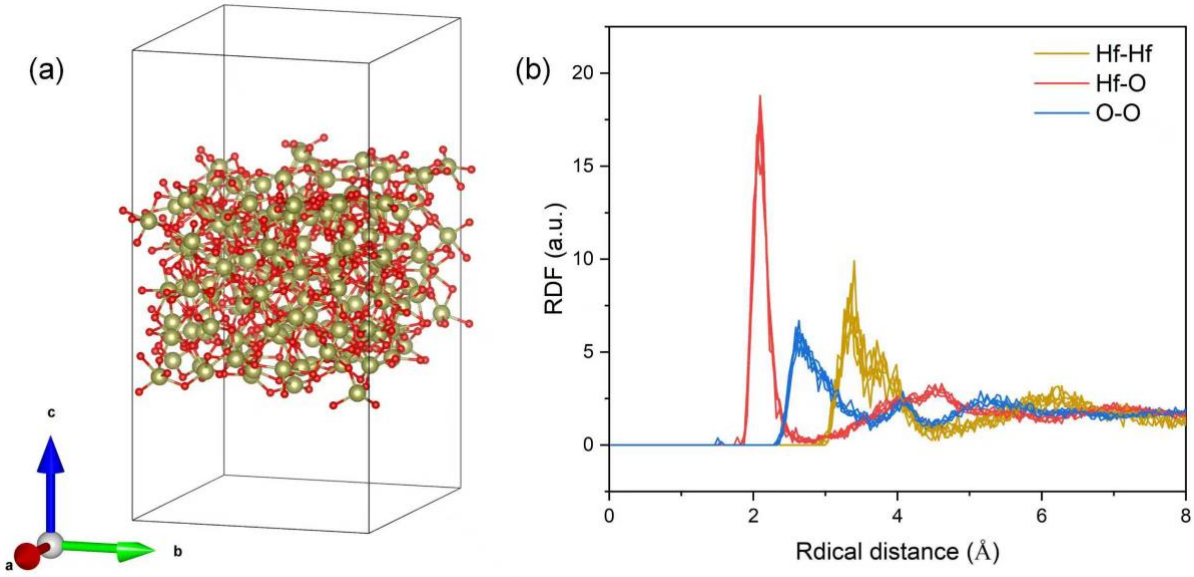

Supplementary Fig. 2 | a, The structure and **b**, Radial distribution functions (RDF) of 5 perfect HfO_2 systems.

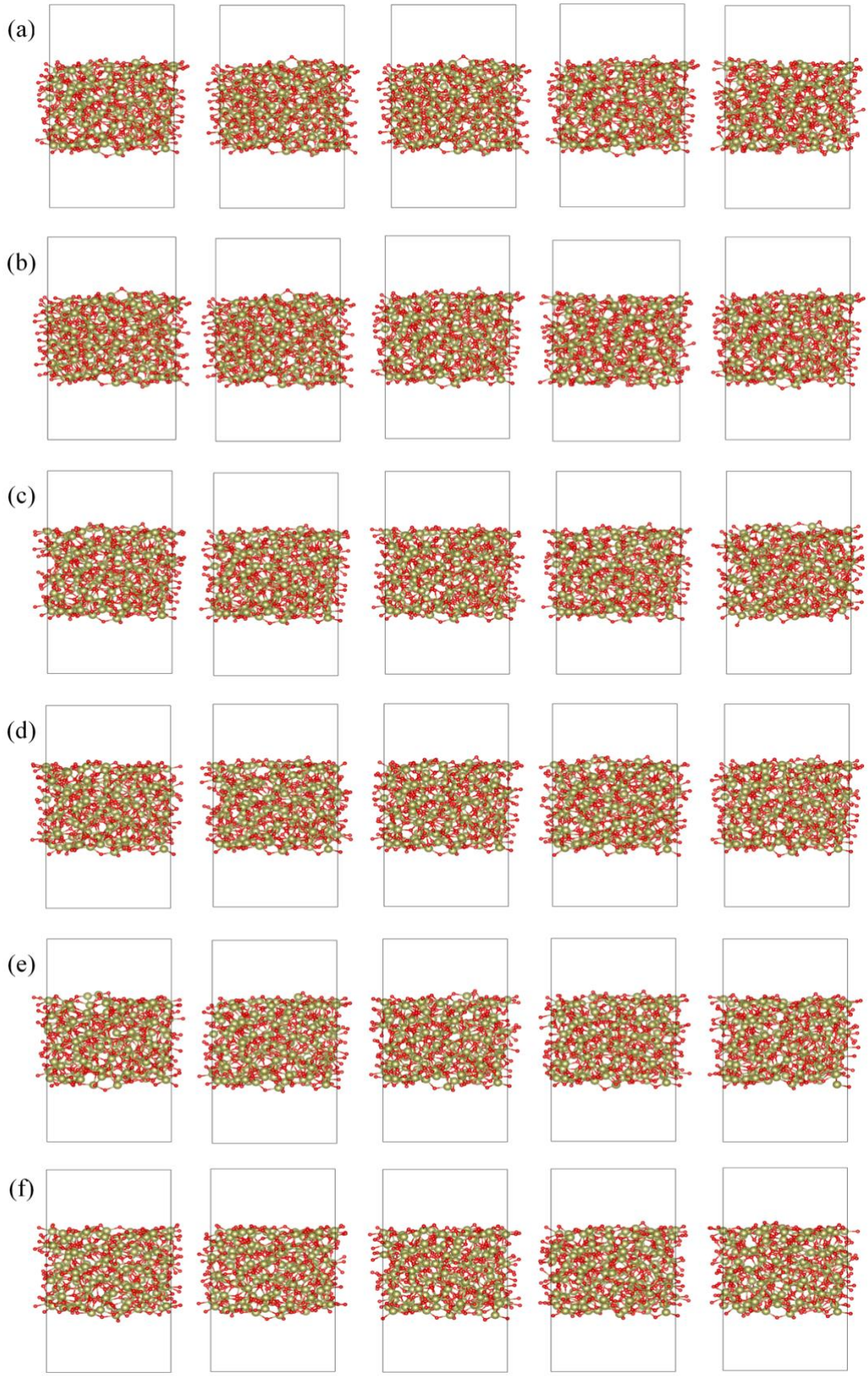

Supplementary Fig. 3 | The amorphous structures of the HfO_2 slabs with different O vacancies concentrations. **a**, perfect, **b**, 2.2%, **c**, 4.4%, **d**, 7.2%, **e**, 10% and **f**, 15.6%.

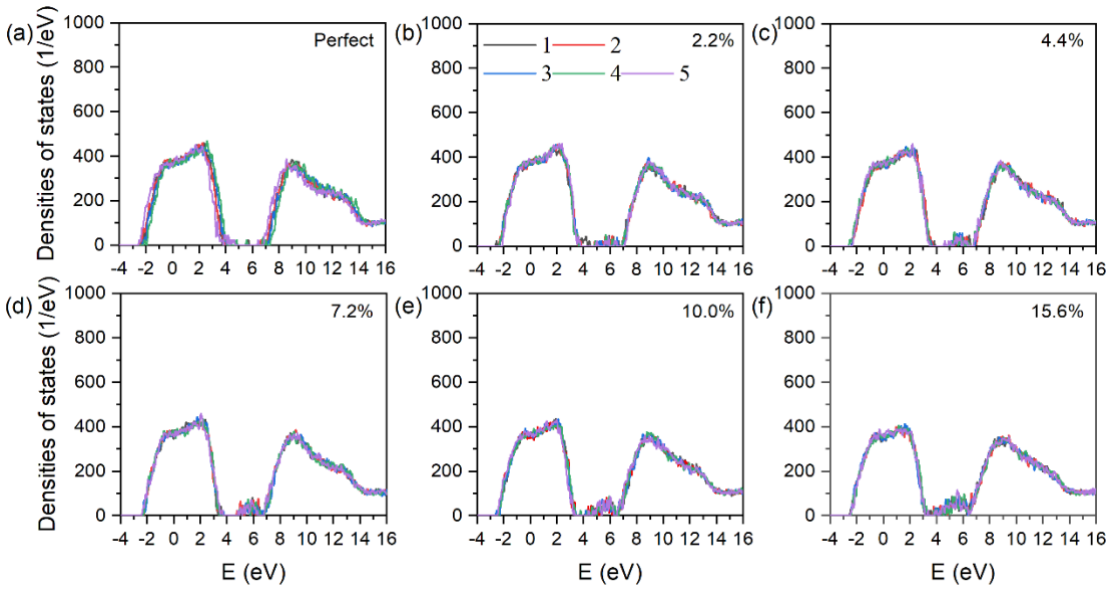

Supplementary Fig. 4 | The density of states of HfO_2 slabs with different O vacancy concentrations calculated by considering PBE functional. For each vacancy concentration, five different random structures are considered. **a,** 0%, **b**, 2.2%, **c**, 4.4%, **d**, 7.2%, **e**, 10% and **f**, 15.6%.

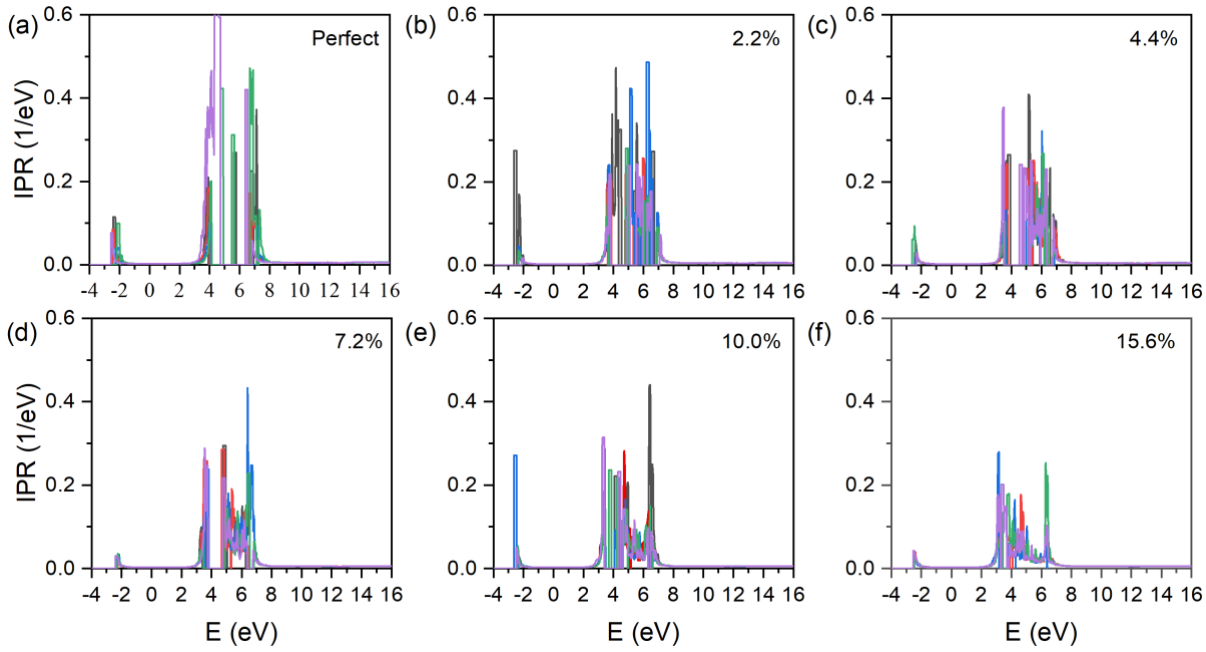

Supplementary Fig. S5 | The Inverse participation ratio (IPR) value for the densities of states of the HfO_2 slabs at different O vacancies concentrations.

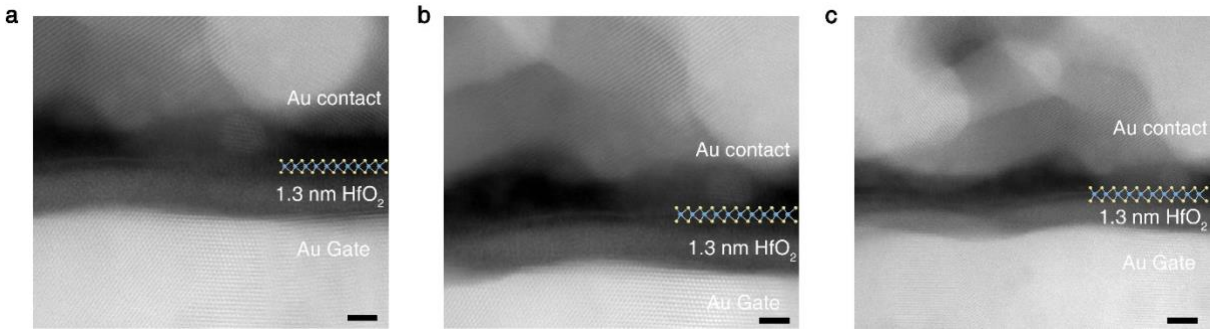

Supplementary Fig. 6 | Cross-sectional STEM image of 2.5-Å-EOT HfO_2 film in three different areas in Fig 1C.

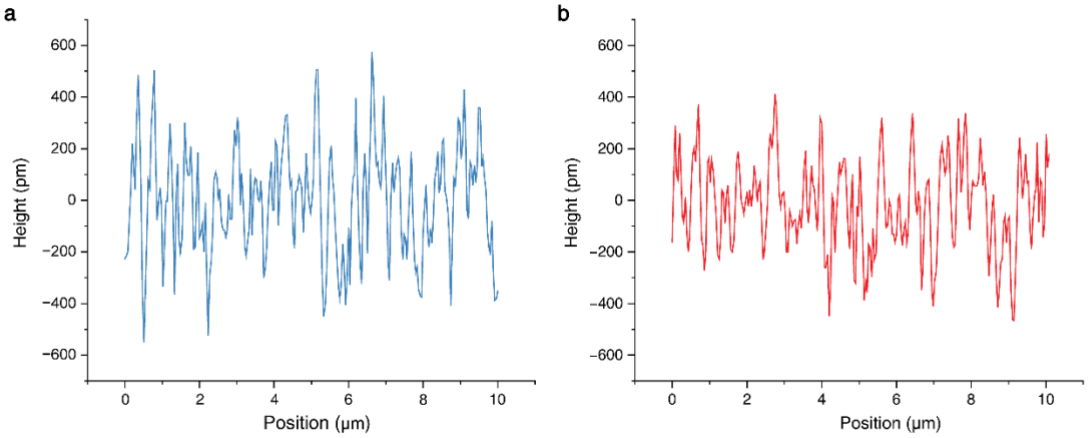

Supplementary Fig. 7 | Line-scan tomography across the 10 μm-length in Fig. 1i

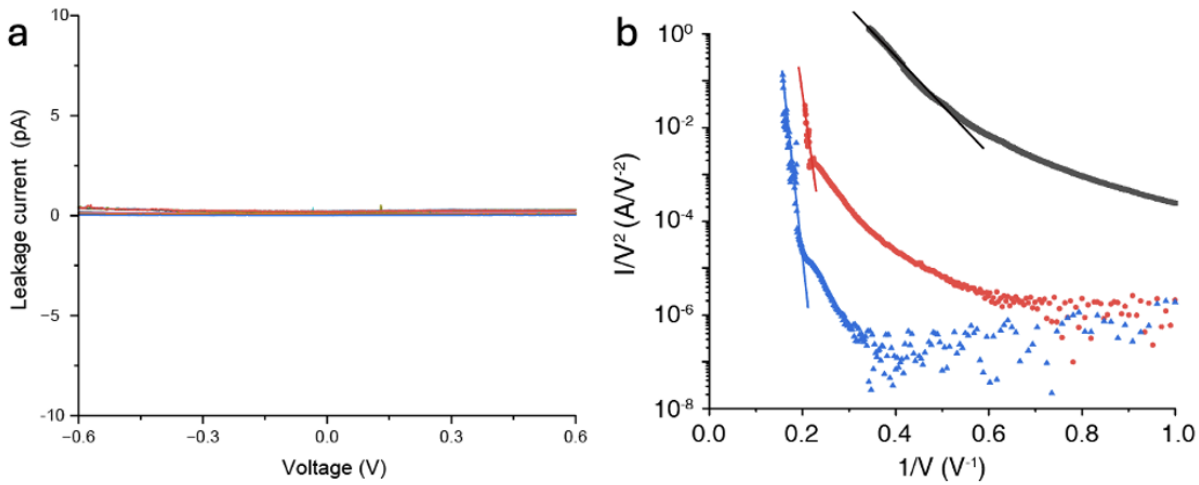

Supplementary Fig. 8 | a, current leakage corresponding with C-V measurement. **b**, Breakdown mechanism of F-N tunneling in 1.3 nm (black), 2.6 nm (red) and 3.9 nm (blue) HfO_2 film. The thickness here represents physical thickness.

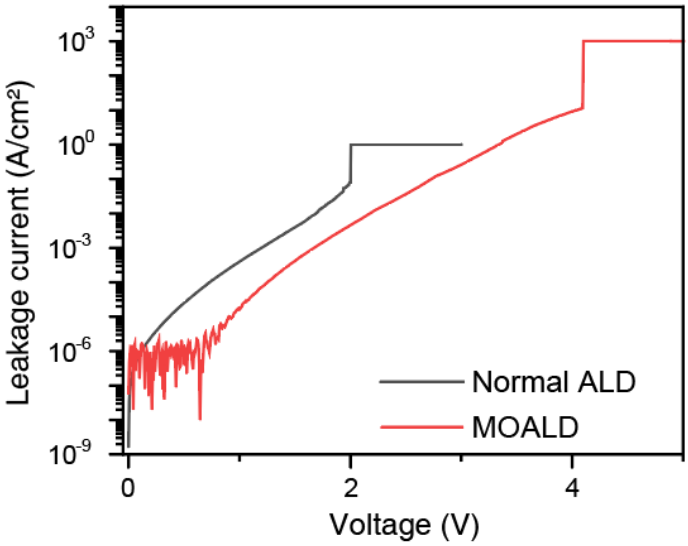

Supplementary Fig. 9 | The breakdown properties of MOALD and normal 1.3 nm (physical thickness) HfO_2 dielectrics.

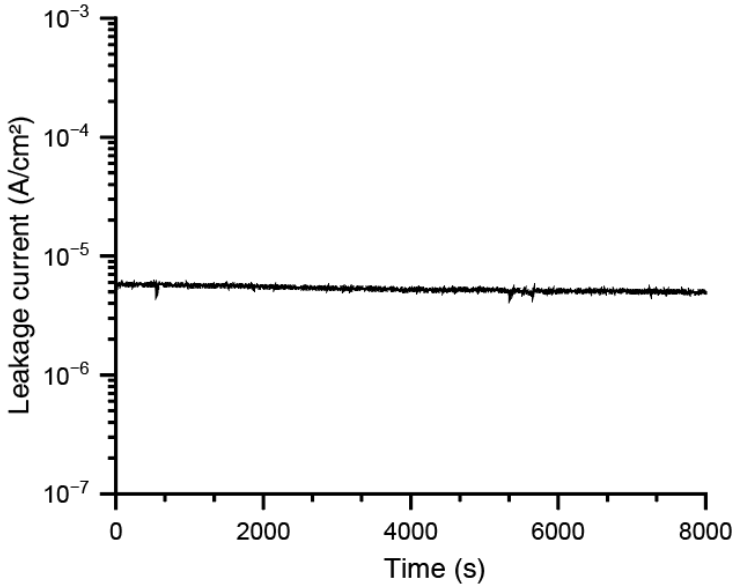

Supplementary Fig. 10 | The electrical stability of 2.5-Å-EOT HfO_2 film under 1.0 V bias.

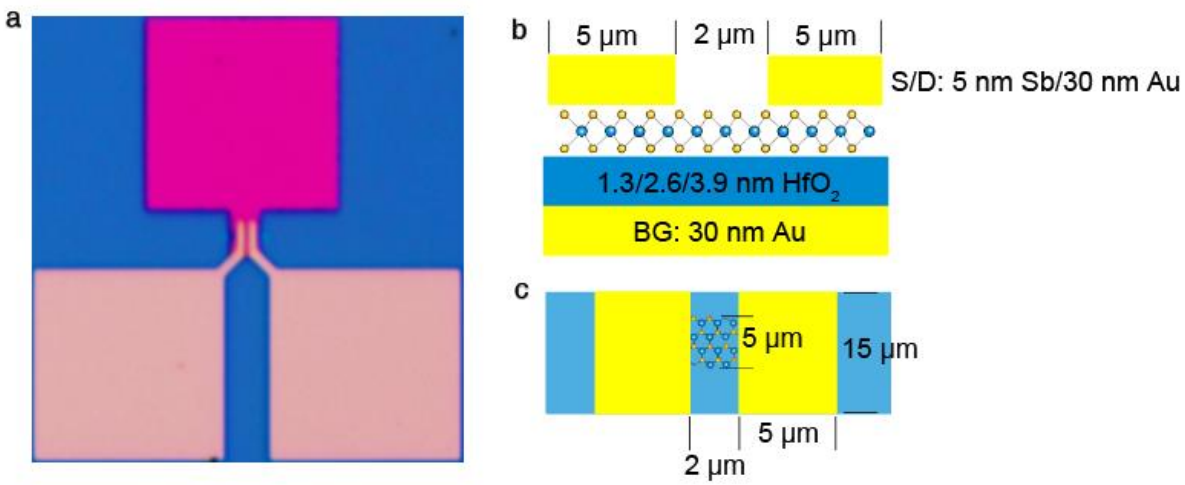

Supplementary Fig. 11 | a, Optical images of μm-length MoS_2 devices. Schematic illustrations of **b**, side-view and **c**, top view of MoS_2 devices in a.

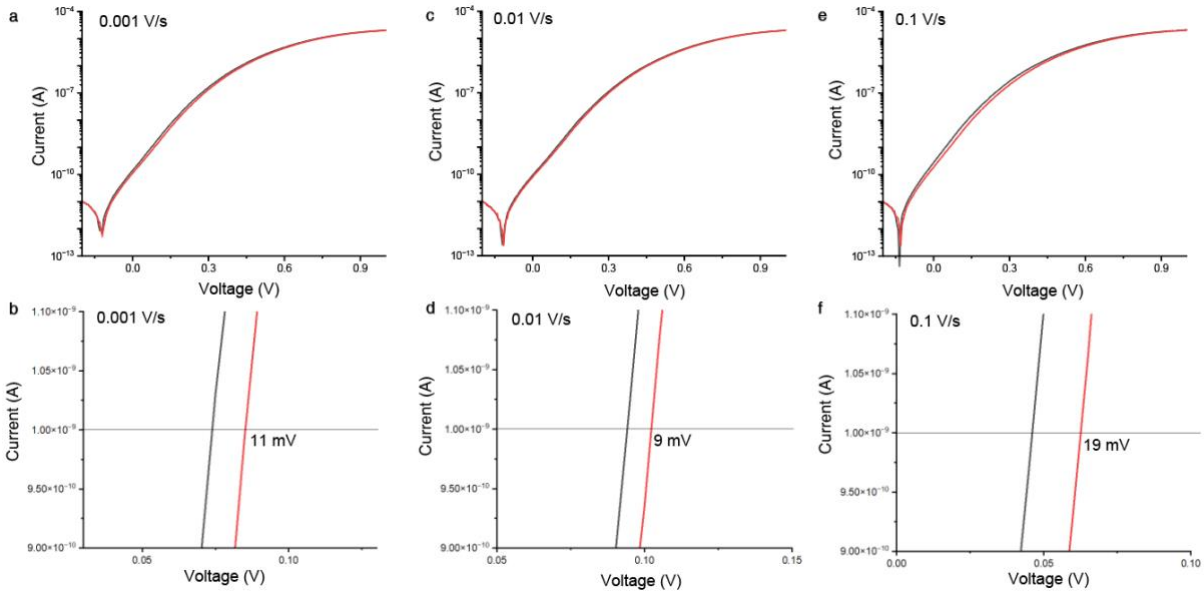

Supplementary Fig. 12 | Bidirectional transfer curve of MoS_2 FETs with 2.5-Å-EOT MOALD HfO_2 with V_{ds} of 0.1 V at sweep frequencies of **a**, 0.001 V/s, **c**, 0.01 V/s and **e**, 0.1 V/s. **b**, d, f, Corresponding hysteresis at 1 nA for a, c and e, respectively.

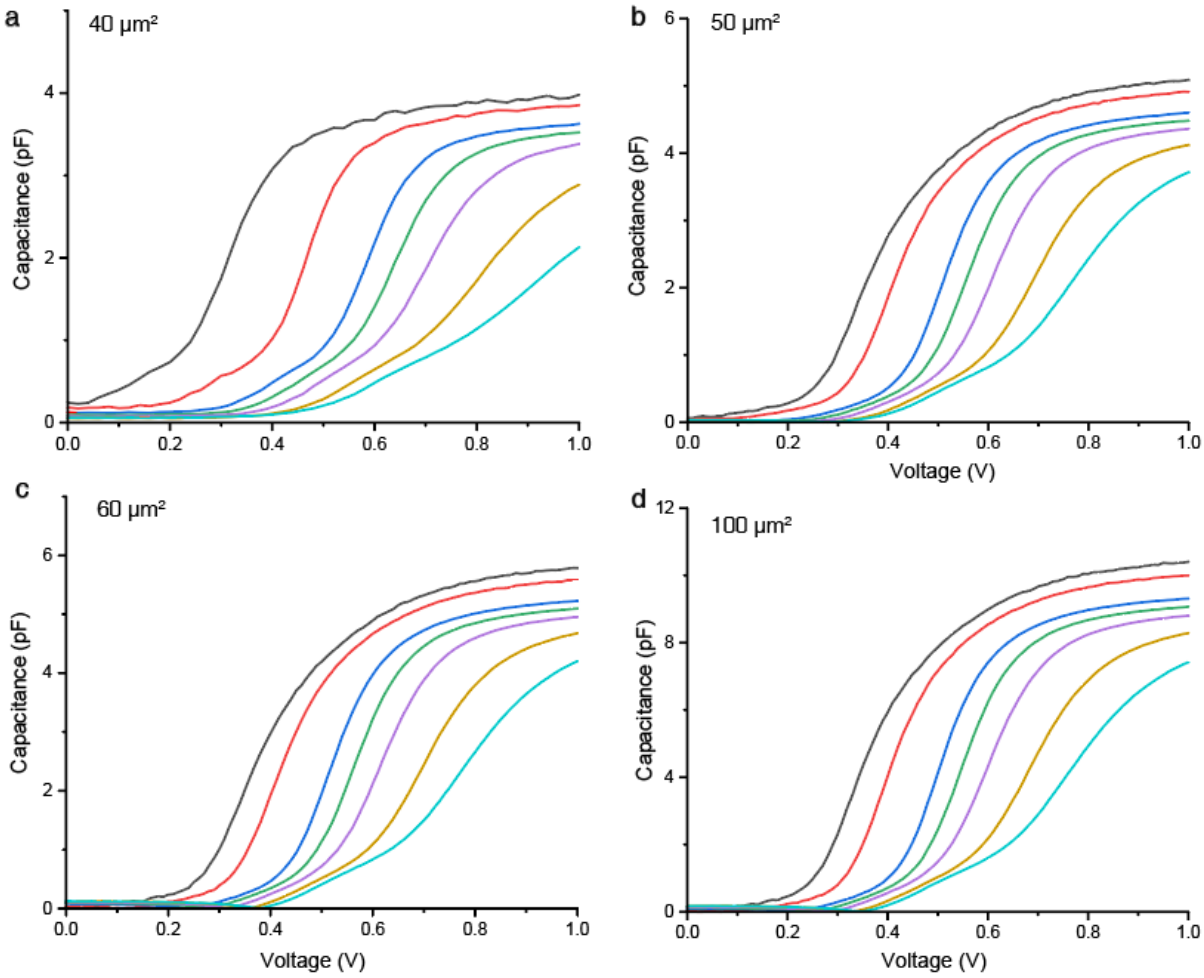

Supplementary Fig. 13 | Effective capacitance tested in MoS_2 gate-first transistors with 1.3 nm HfO_2 dielectrics. Frequencies vary from 5 kHz to 1 MHz in devices with various areas from (a) 40 μm^2 to (d) 100 μm^2.

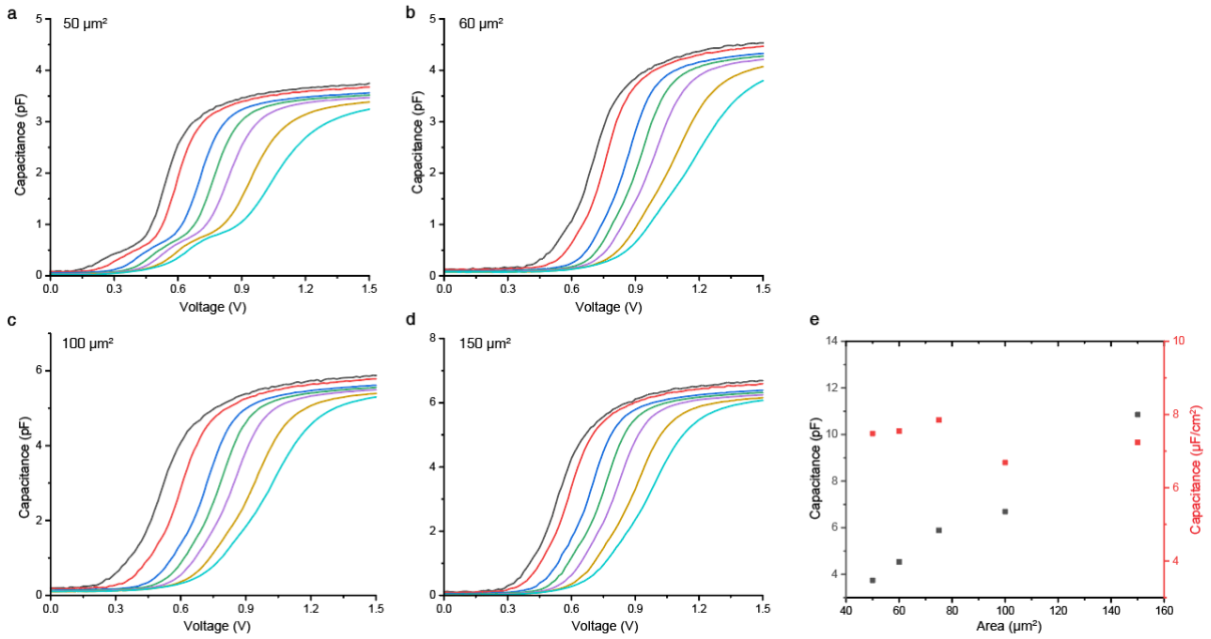

Supplementary Fig. 14 | Effective capacitance tested in MoS_2 gate-first transistors with 2.6 nm HfO_2 dielectrics. Frequencies vary from 5 kHz to 1 MHz in devices with various areas from (a) 40 μm^2 to (d) 200 μm^2. (e) Statistic capacitance and normalized capacitance for all five devices

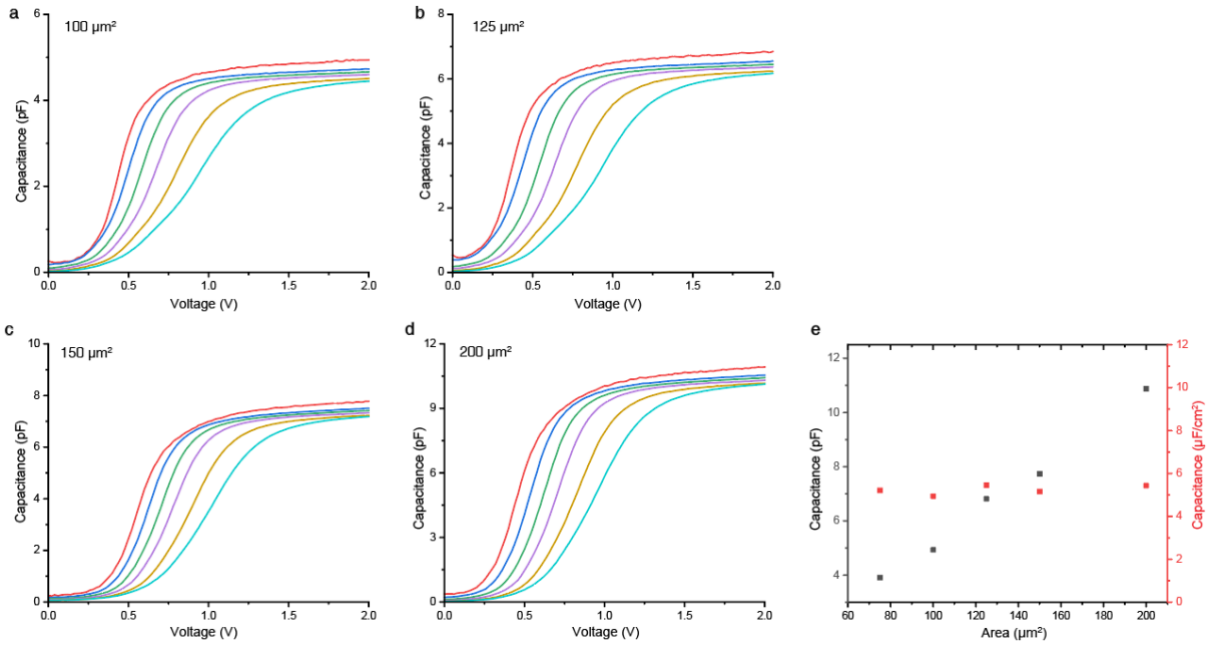

Supplementary Fig. 15 | Effective capacitance tested in MoS_2 gate-first transistors with 3.9 nm HfO_2 dielectrics. Frequencies vary from 5 kHz to 1 MHz in devices with various areas from (a) 10 μm^2 to (e) 200 μm^2. (e) Statistic capacitance and normalized capacitance for all five devices

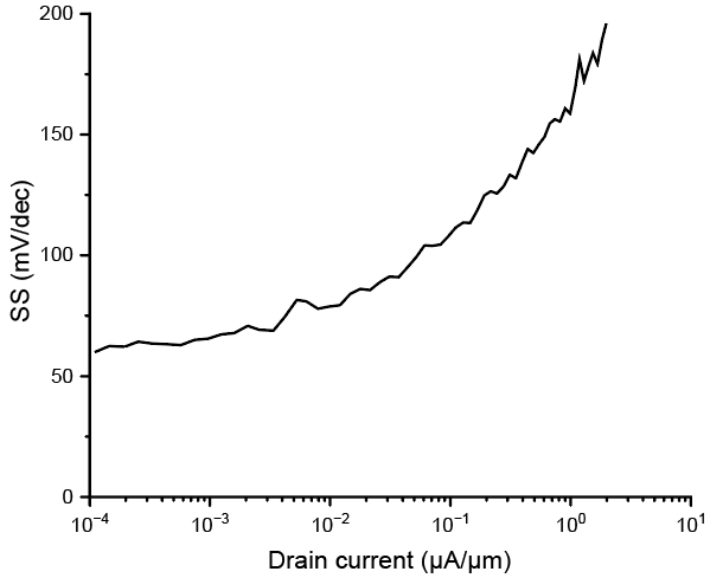

Supplementary Fig. 16 | Corresponding subthreshold swing curve with 0.1 V source-drain bias in 100-nm channel length MoS_2 FETs.

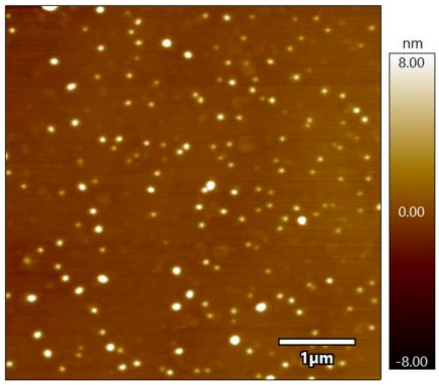

Supplementary Fig. 17 | AFM tomography for MOALD HfO_2 directly on MoS_2. HfO_2 forms an island of particles rather than a continuous film.

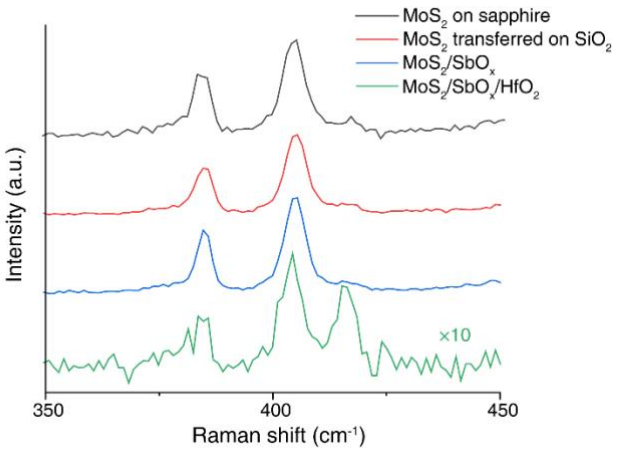

Supplementary Fig. 18 | Raman spectra of MoS_2 on sapphire, transferred on SiO_2 substrate, after depositing SbO_x seeding layer and MOALD HfO_2 dielectrics.

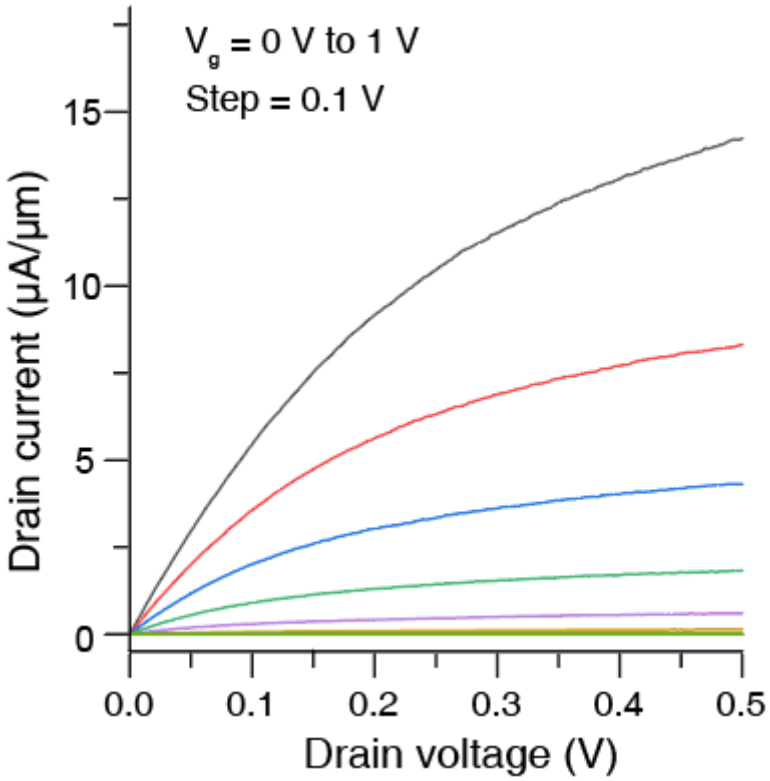

Supplementary Fig. 19 | Output curves of MoS_2 gate-last transistors with ultrathin dielectrics.

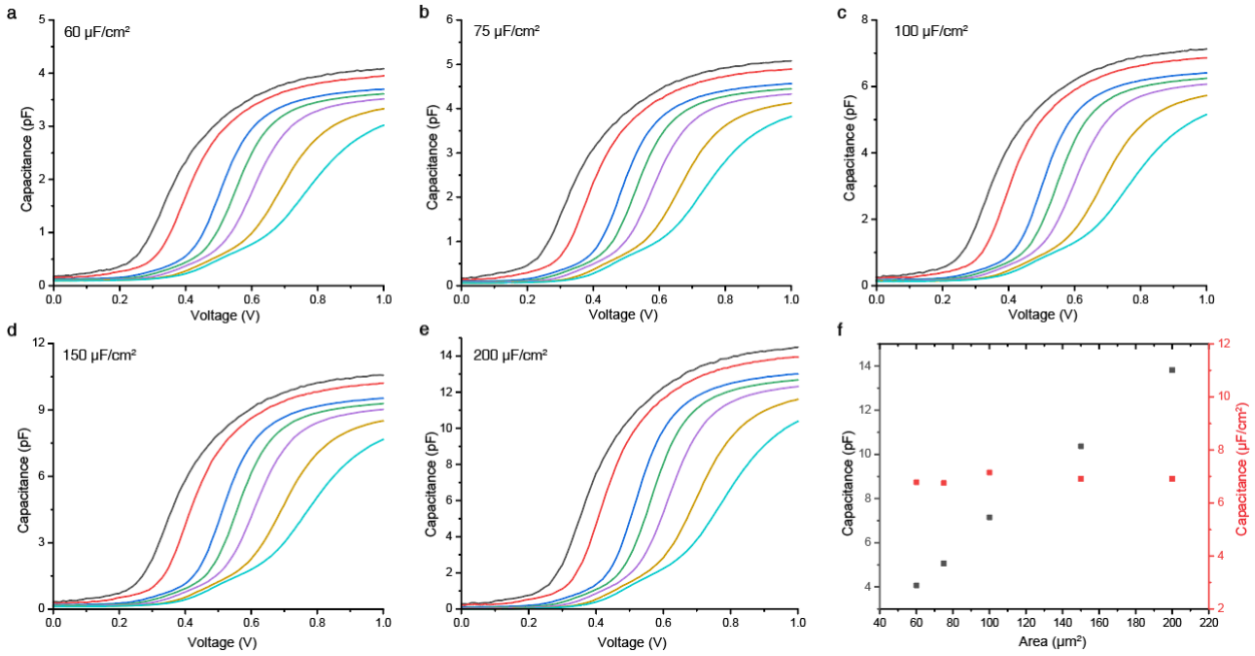

Supplementary Fig. 20 | Effective capacitance tested in MoS_2 gate-last transistors with 1 nm SbO_x seeding layer and 1.3 nm HfO_2 dielectrics. Frequencies vary from 5 kHz to 1 MHz in devices with various areas from (a) 60 μm^2 to (e) 200 μm^2. (f) Statistic capacitance and normalized capacitance for all five devices

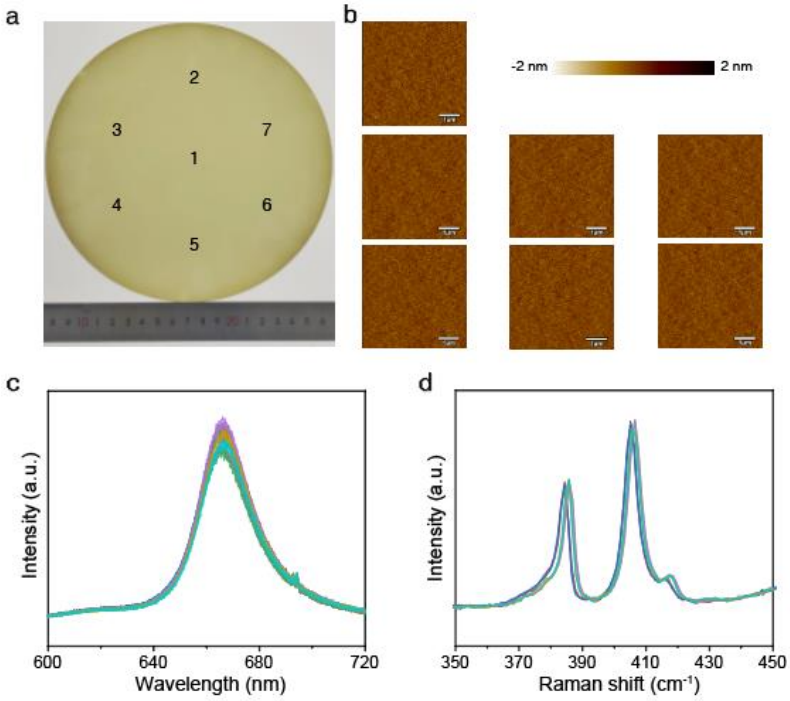

Supplementary Fig. 21 | The characterization of 8-inch MoS_2 samples. Each measurement was tested from 7 different points. **a**, Optical images 8-inch MoS_2 wafers. **b**, AFM, **c**, PL and **d**, Raman spectra of 7 points marked in a.

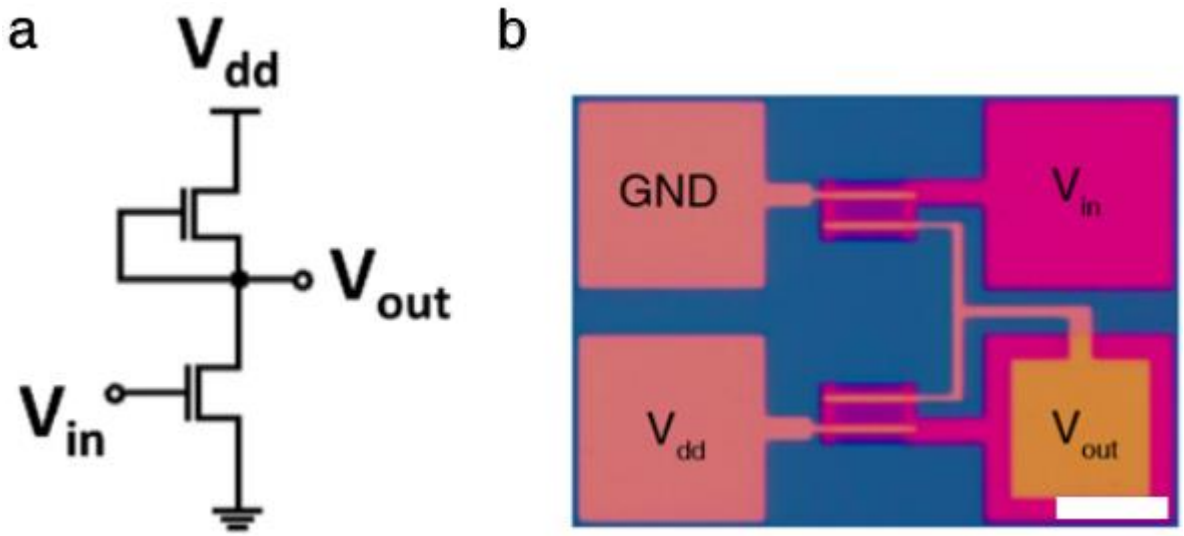

Supplementary Fig. 22 | a, Equivalent circuit and **b**, true device for an all-NMOS inverter. scale bar: 50μm

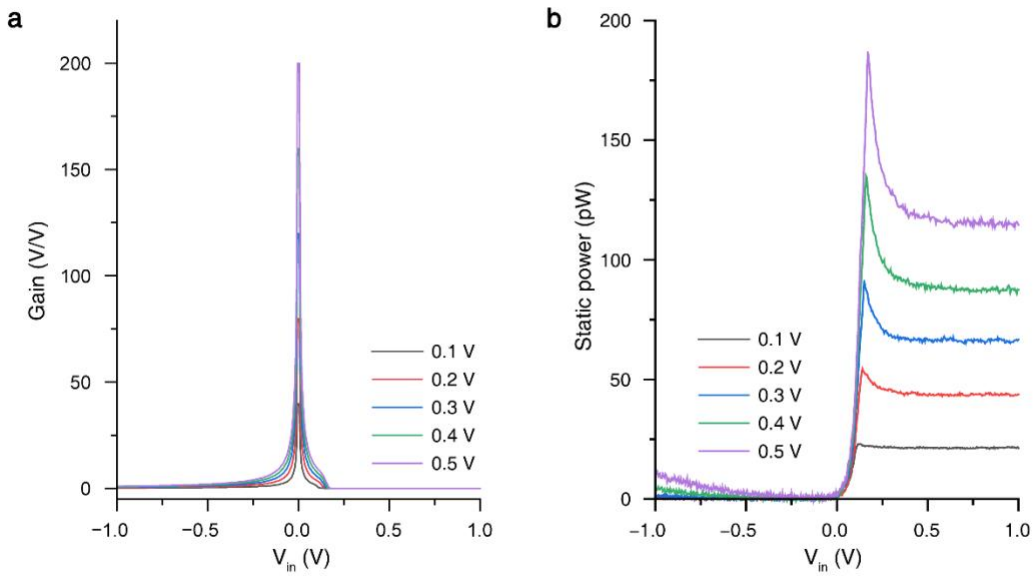

Supplementary Fig. 23 | a, Gain and **b**, Static power measurement in Fig. 5f.

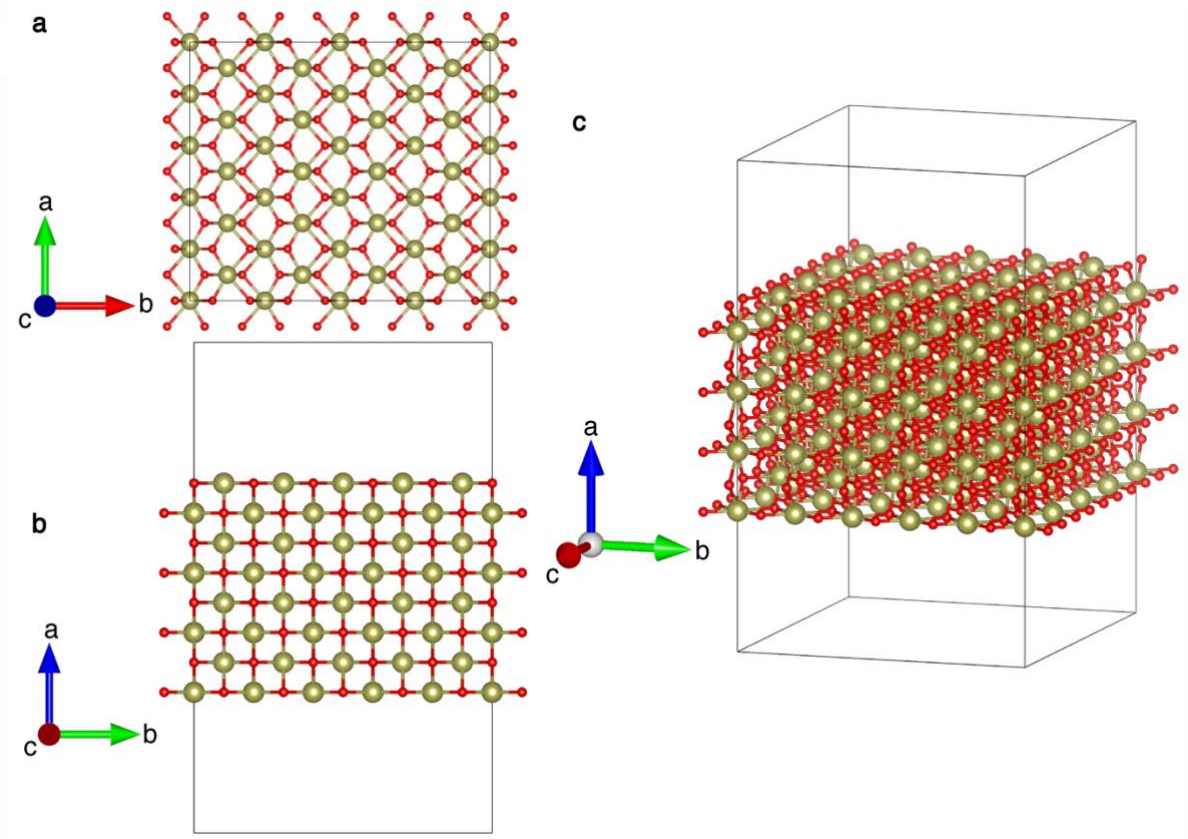

Supplementary Fig. 24 | The (a) top, (b) side and (c) perspective views of HfO_2 slab model.

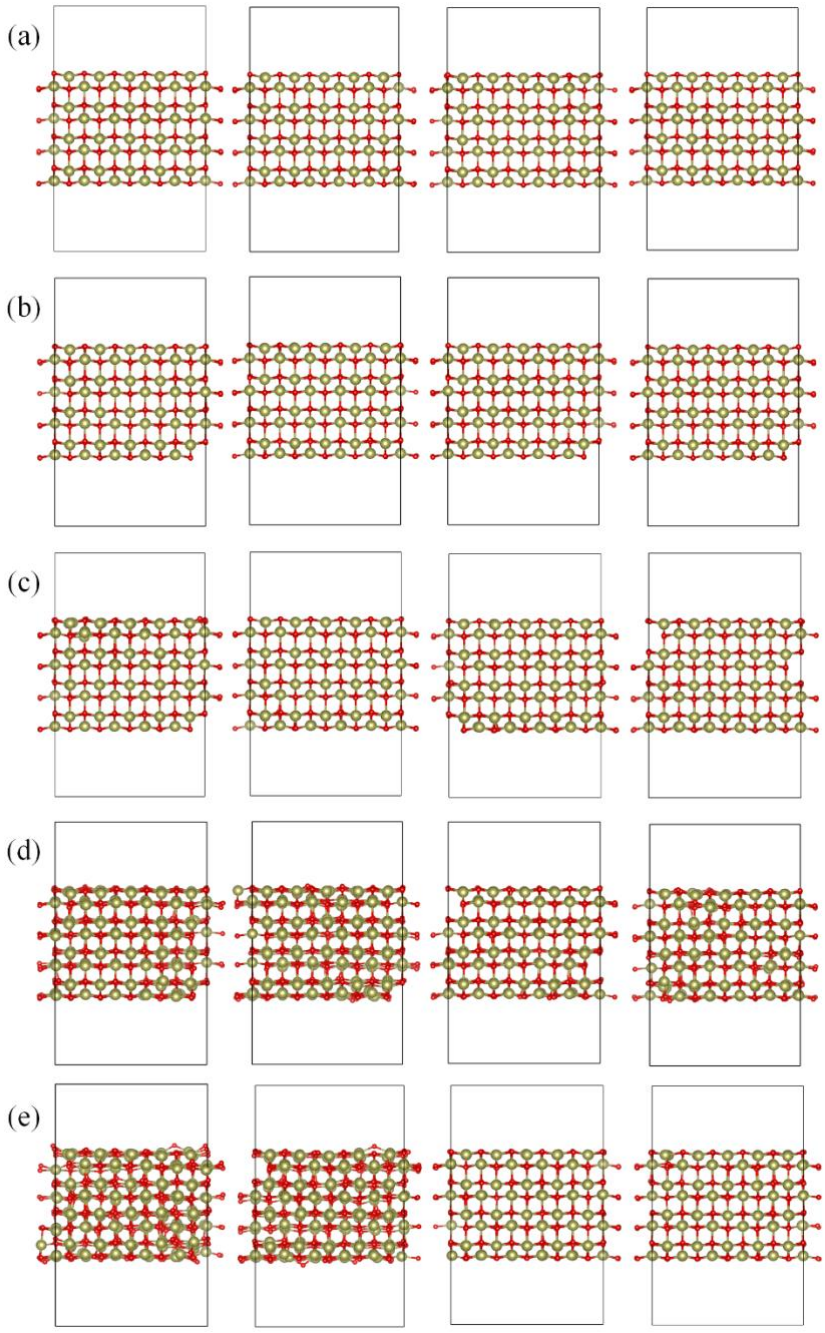

Supplementary Fig. 25 | The optimized structures of HfO_2 slabs with different vacancy concentrations. **a**, 2.2%, **b**, 4.4%, **c**, 7.2%, **d**, 10% and **e**, 15.6%.

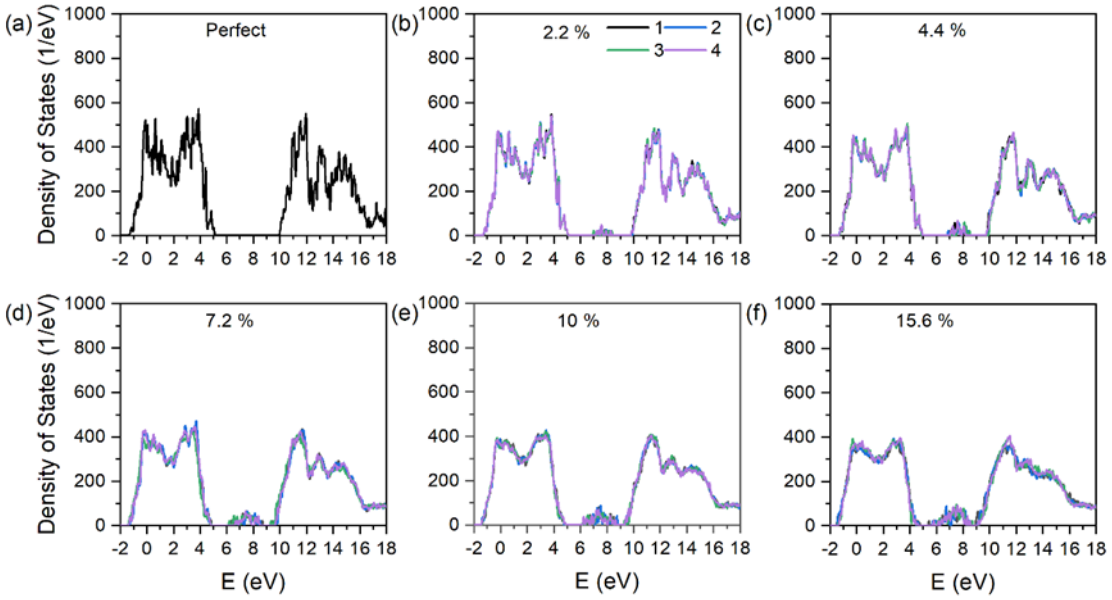

Supplementary Fig. 26 | The density of states of HfO_2 slabs with different O vacancy concentrations calculated by considering HSE06 functional. For each vacancy concentration, five different random structures are considered. **a,** 0%, **b**, 2.2%, **c**, 4.4%, **d**, 7.2%, **e**, 10% and **f**, 15.6%.

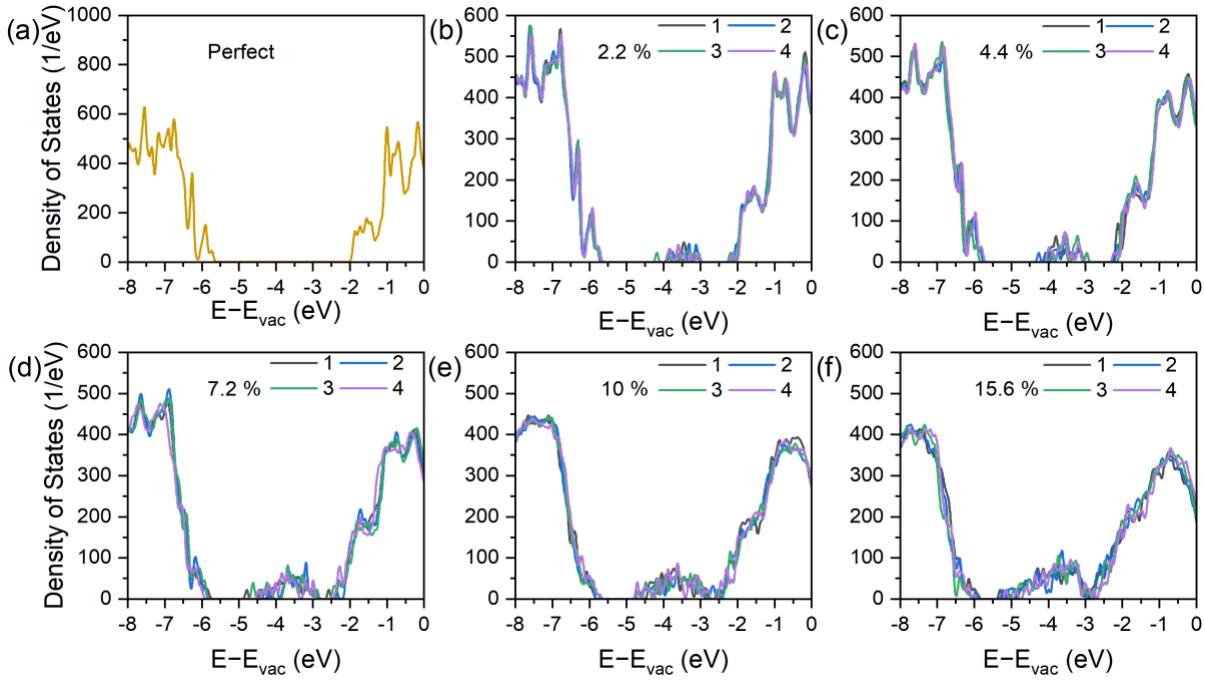

Supplementary Fig. 27 | The density of states of HfO_2 slabs with different O vacancy concentrations calculated by considering PBE functional. For each vacancy concentration, five different random structures are considered. The energy has been aligned by setting the vacuum level E_{vac} of each system at zero. **a,** 0%, **b**, 2.2%, **c**, 4.4%, **d**, 7.2%, **e**, 10% and **f**, 15.6%.

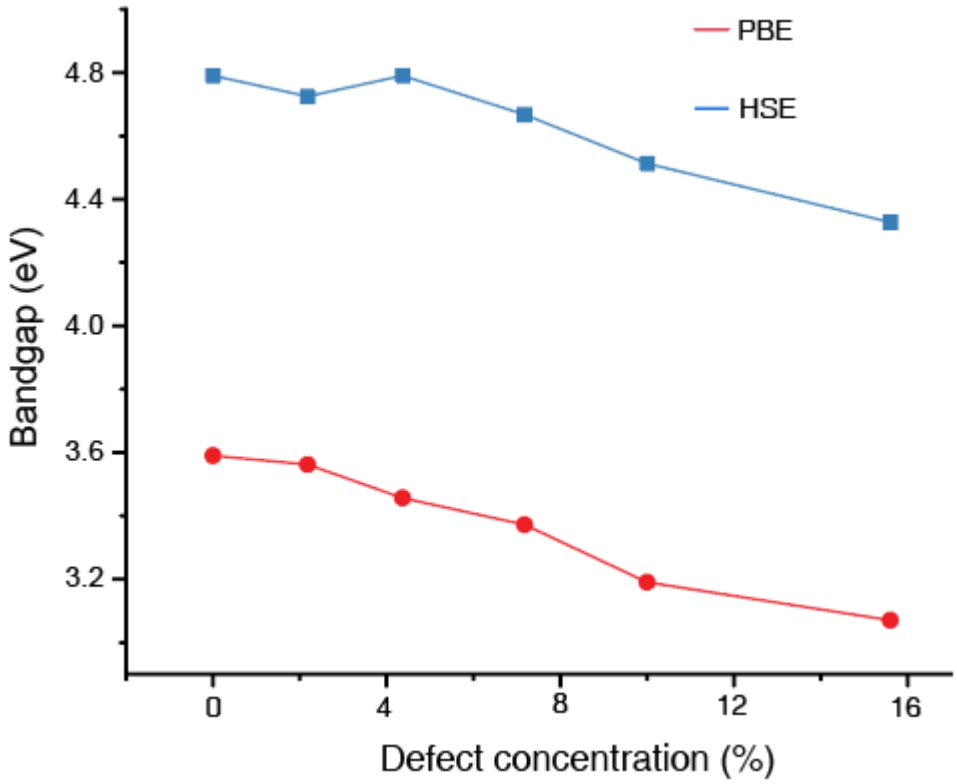

Supplementary Fig. 28 | The bandgaps of HfO_2 slabs with different O_v defect concentrations calculated by considering PBE and HSE06 functionals.

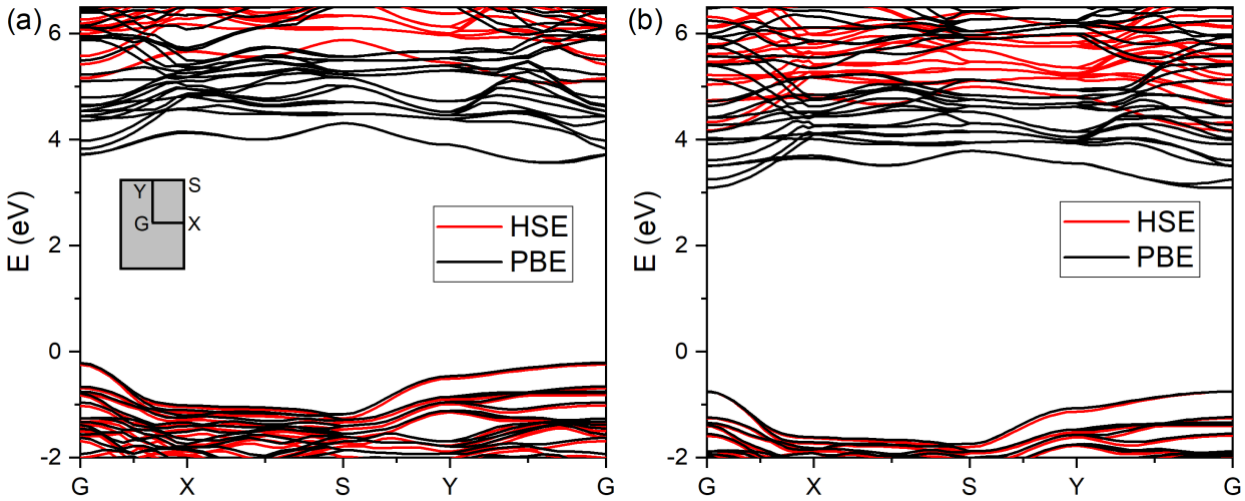

Supplementary Fig. 29 | The band structures of perfect HfO_2 slab system calculated by (a) VASP and (b) ABACUS.

Supplementary Table 1 | The measured bandgaps from densities of states of the HfO_2 slabs without O vacancies concentrations.

Structure	VBME (PBE)	CBME (PBE)	ME_g (PBE)
1	3.535	7.095	3.560
2	3.665	7.060	3.395
3	3.800	7.405	3.605
4	4.285	7.260	2.975
5	3.945	7.035	3.090
Average	3.846	7.171	3.325

Supplementary Table 2 | the measured bandgaps from densities of states of the HfO_2 slabs with 2.2% O vacancies concentrations.

Structure	VBME (PBE)	CBME (PBE)	ME_g (PBE)
1	3.545	6.195	2.650
2	3.455	6.095	2.640
3	3.415	6.215	2.800
4	3.535	6.115	2.580
5	3.530	6.195	2.665
Average	3.496	6.163	2.667

Supplementary Table 3 | the measured bandgaps from densities of states of the HfO_2 slabs with 4.4% O vacancies concentrations.

Structure	VBME (PBE)	CBME (PBE)	ME_g (PBE)
1	3.565	6.305	2.740
2	3.490	6.195	2.705
3	3.375	6.135	2.760
4	3.330	6.190	2.860
5	3.285	5.900	2.615
Average	3.409	6.145	2.736

Supplementary Table 4 | the measured bandgaps from densities of states of the HfO_2 slabs with 7.2% O vacancies concentrations.

Structure	VBME (PBE)	CBME (PBE)	ME_g (PBE)
1	3.355	6.030	2.675
2	3.355	5.940	2.585
3	3.410	6.140	2.730
4	3.255	6.070	2.815
5	3.405	5.995	2.590
Average	3.356	6.035	2.679

Supplementary Table 5 | the measured bandgaps from densities of states of the HfO_2 slabs with 10% O vacancies concentrations.

Structure	VBME (PBE)	CBME (PBE)	ME_g (PBE)
1	3.300	5.645	2.345
2	3.335	5.695	2.360
3	3.360	5.555	2.195
4	3.425	5.705	2.280
5	3.240	5.650	2.410
Average	3.332	5.650	2.318

Supplementary Table 6 | the measured bandgaps from densities of states of the HfO_2 slabs with 15.6% O vacancies concentrations.

Structure	VBME (PBE)	CBME (PBE)	ME_g (PBE)
1	3.230	5.355	2.125
2	3.050	5.380	2.330
3	2.905	5.385	2.480
4	3.130	5.350	2.220
5	3.175	5.360	2.185
Average	3.098	5.366	2.268

Supplementary Table 7 | Benchmark of dielectrics with sub-3-nm EOT for transistors.

Dielectric	EOT (nm)	Current leakage(A/cm^2)	Reference
Al_2O_3	2.5	N/A	8
ZrO_2	2.4	10^{-2}	9
HfO_2	1.9	10^{-1}	10
Sb_2O_3	1.6	10^{-7}	11
Bi_2SiO_5	1.3	10^{-5}	12
HfO_x	1.1	10^{-5}	13
Er_2O_3	1.1	10^{-6}	14
HfO_2	1	10^{-2}	15
PTCDA/HfO_2	1	10^{-2}	16
CaF_2	1	10^{-3}	17
$SrTiO_3$	1	1	18
HfO_2-ZrO_2 superlattice	0.75	10^{-1}	19
HfO_2	0.73	N/A	20
Sb_2O_3/HfO_2	0.67	10^{-7}	21
HfO_2-ZrO_2 superlattice	0.65	10^{-1}	22
La-silicate	0.62	10	23
Bi_2SeO_5	0.41	10^{-2}	24
GdOCl	1.3	10^{-6}	25
Gd_2O_5	0.94	10^{-7}	26
Ga_2O_3	0.4	10^{-4}	27
$MgNb_2O_6$	1	10^{-6}	28
MOALD HfO_2	0.27	10^{-6}	This work

Supplementary Reference

1. Mora-Fonz, D. *et al.* Disorder-induced electron and hole trapping in amorphous TiO_2. *Phys. Rev. B* **102**, 054205 (2020).
2. Kaewmeechai, C. *et al.* Electronic structure an properties of trapped holes in crystalline and amorphous Ga_2O_3. *Phys. Rev. B* **111**, 035203 (2025).
3. El-Sayed, A. *et al.* Nature of intrinsic and extrinsic electron trapping in SiO_2. *Phys. Rev. B* **89**, 125201 (2014).
4. Xie, Y. *et al.* Hybrid density functional study of structural and electronic properties of functionalized $Ti_{n+1}X_n$ (X= C, N) monolayers. *Phys. Rev. B* **87**, 235441 (2013).
5. Flores, E. *et al.* Structural and electronic properties of bulk ZnX (X= O, S, Se, Te), ZnF_2, and ZnO/ZnF_2: A DFT investigation within PBE, PBE+U, and hybrid HSE functionals. *J. Phys. Chem. A* **124**, 3778-3785 (2020).
6. Heyd, J. *et al.* Hybrid functionals based on a screened Coulomb potential. *J. Chem. Phys.* **118**, 8207-8215 (2003).
7. Kresse, G. *et al.* Efficient iterative schemes for ab initio total-energy calculations using a plane-wave basis set. *Phys. Rev. B* **54**, 11169 (1996).
8. English, C. D. *et al.* Approaching ballistic transport in monolayer MoS_2 transistors with self-aligned 10 nm top gates. *2016 IEEE Int. Electron Devices Meet. (IEDM)*, 5.6.1-5.6.4 (2016).
9. Jin, Y. *et al.* Controllable Oxidation of ZrS_2 to Prepare High-κ, Single-Crystal m-ZrO_2 for 2D Electronics. *Adv. Mater.* **35**, e2212079 (2023).
10. Smets, Q. *et al.* Ultra-scaled MOCVD MoS_2 MOSFETs with 42nm contact pitch and 250μA/μm drain current. *2019 IEEE Int. Electron Devices Meet. (IEDM)* **00**, 23.2.1-23.2.4 (2019).
11. Liu, K. *et al.* A wafer-scale van der Waals dielectric made from an inorganic molecular crystal film. *Nat Electron* **4**, 906–913 (2021).
12. Chen, J. *et al.* Vertically grown ultrathin Bi_2SiO_5 as high-κ single-crystalline gate dielectric. *Nat. Commun.* **14**, 4406 (2023).
13. Luo, P. *et al.* Molybdenum disulfide transistors with enlarged van der Waals gaps at their dielectric interface via oxygen accumulation. *Nat. Electron.* **5**, 849–858 (2022).
14. Uchiyama, H. *et al.* A Monolayer MoS_2 FET with an EOT of 1.1 nm Achieved by the Direct Formation of a High-κ Er_2O_3 Insulator Through Thermal Evaporation. *Small* **19**, e2207394 (2023).
15. Pang, C.-S. *et al.* Sub-1nm EOT WS_2-FET with IDS > 600μA/μm at V_{DS}=1V and SS < 70mV/dec at LG=40nm. *2020 IEEE Int. Electron Devices Meet. (IEDM)* **00**, 3.4.1-3.4.4 (2020).
16. Li, W. *et al.* Uniform and ultrathin high-κ gate dielectrics for two-dimensional electronic devices. *Nat Electron* **2**, 563–571 (2019).
17. Illarionov, Y. Yu. *et al.* Ultrathin calcium fluoride insulators for two-dimensional field-effect transistors. *Nat Electron* **2**, 230–235 (2019).
18. Huang, J.-K. *et al.* High-κ perovskite membranes as insulators for two-dimensional transistors. *Nature* **605**, 262–267 (2022).

19. Li, W. *et al.* S. Salahuddin, Demonstration of Low EOT Gate Stack and Record Transconductance on Lg=90 nm nFETs Using 1.8 nm Ferroic HfO_2-ZrO_2 Superlattice. *2021 IEEE Int. Electron Devices Meet. (IEDM)* **00**, 13.6.1-13.6.4 (2021).
20. Chiang, C.-C. *et al.* Air-Stable P-Doping in Record High-Performance Monolayer WSe_2 Devices. IEEE Electron Device Lett. 43, 319–322 (2022).
21. Xu, Y. *et al.* Scalable integration of hybrid high-κ dielectric materials on two-dimensional semiconductors. *Nat. Mater.* **22**, 1078–1084 (2023).
22. Cheema, S. S. *et al.* Ultrathin ferroic HfO_2–ZrO_2 superlattice gate stack for advanced transistors. *Nature* **604**, 65–71 (2022).
23. Kawanago, T. *et al.* EOT of 0.62 nm and High Electron Mobility in La-silicate/Si Structure Based nMOSFETs Achieved by Utilizing Metal-Inserted Poly-Si Stacks and Annealing at High Temperature. *IEEE Trans. Electron Devices* **59**, 269–276 (2012).
24. Zhang, Y. *et al.* A single-crystalline native dielectric for two-dimensional semiconductors with an equivalent oxide thickness below 0.5 nm. *Nat. Electron.* **5**, 643–649 (2022).
25. Xu, W. *et al.* Single-crystalline High-κ GdOCl dielectric for two-dimensional field-effect transistors. *Nat. Commun.* **15**, 9469 (2024).
26. Yin, L. *et al.* High-κ monocrystalline dielectrics for low-power two-dimensional electronics. *Nat. Mater.* **24**, 197–204 (2025).
27. Yi, K. *et al.* Integration of high-κ native oxides of gallium for two-dimensional transistors. *Nat. Electron.* **7**, 1126–1136 (2024).
28. Zhu, C.-Y. *et al.* Magnesium niobate as a high-κ gate dielectric for two-dimensional electronics. *Nat. Electron.* **7**, 1137–1146 (2024).